Asymmetries in the Electronic Properties of Spheroidal Metallic Nanoparticles, Revealed by Conduction Electron Spin Resonance and Surface Plasmon Resonance

Santina S. Cruz, Vadim Tanygin, and Benjamin J. Lear*

Department of Chemistry, The Pennsylvania State University, University Park, 16802, U.S.A.

E-mail: bul14@psu.edu

Phone: (814) 867-4625

Abstract

Using electron spin resonance spectroscopy, we demonstrate that the morphological asymmetries present in small spheroidal metallic nanoparticles gives rise to asymmetries in the behavior of electrons held in states near the metal's Fermi energy. We find that the effects of morphological asymmetries for these spheroidal systems are more important than the effects of size distributions, when explaining the asymmetry in electronic behavior. This is found to be true for all the particles examined, which were made from Cu, Ag, Pd, Ir, Pt, and Au, bearing dodecanethiolate ligands. In the case of the Ag particles, we also demonstrate that the same model used to account for morphological effects in the electron spin resonance spectra can be used to account for small asymmetries present in the plasmon spectrum. This result demonstrates that the electronic properties of even small particles are tunable *via* morphological changes.

Keywords

metallic nanoparticles, electron spin resonance, electron paramagnetic resonance, plasmon, morphology, and magnetic susceptibility

Metallic nanoparticles are a fixture of modern science, where they provide a platform for a wide range of established and emerging technologies, including cancer treatment,[1–3] sensing,[4–6] and catalysis.[7–12] In all of these applications, it is the electronic structure and behavior of the nanoparticles that make them desirable. For example, metallic particles can possess a plasmon resonance that greatly enhance electric fields and allow single molecule sensing,[13] provide hot electrons for electrocatalysis,[14,15] and provide rapid light-to-heat conversion for driving thermally activated chemical transformations.[16–20] Beyond plasmonic-based behaviors, the electronic structure of small particles can provide catalytic activity that differs greatly from bulk or atomic species.[9–12]

The importance of nanoparticle electronic properties has motivated the development of a means to control and tune these properties. One of the most common means of doing so is through physical changes to the metallic core of the particles. In particular, morphology (a.k.a. shape) has emerged as a powerful means to control the behavior of individual particles[21–23] and the coupling between them.[24] As a particle's shape deviates from spheroidal, the particle's electronic structure (Figure 1) and resulting behavior can depend on the direction considered. This has motivated the development of synthetic protocols that target shapes which deviate strongly from spherical, such as rods, triangular prisms, and purposefully twinned particles. These changes in shape have been shown to play a critical role in controlling electronic behaviors of metallic particles, such as plasmon resonance, plasmonic coupling,[25,26] and catalylic activity.[27]

Though synthetic control of particle shape is a powerful tool for tuning the behavior of metallic nanoparticles, it is often only employed for systems with average dimensions well above 5 nm. For smaller systems, their surface energy makes it difficult to produce particles whose morphology deviates strongly from spheres. As a result, it can be difficult to target specific shapes, as such, samples of small particles often encompass a wide range of morphologies loosely categorized as 'spheroidal.' Such spheroidal populations include particles with small differences between them, such as placements of facets and add-atoms. While

larger particles often include similar 'imperfections,' such differences are often insignificant compared to the overall particle dimensions. On the other hand, for small particles, small differences can represent significant morphological changes, but changes that would require detailed high-resolution particle-by-particle analysis to characterize. While this analysis is technically possible using modern techniques, such as TEM, it is extremely time consuming and is generally not pursued without strong motivations.

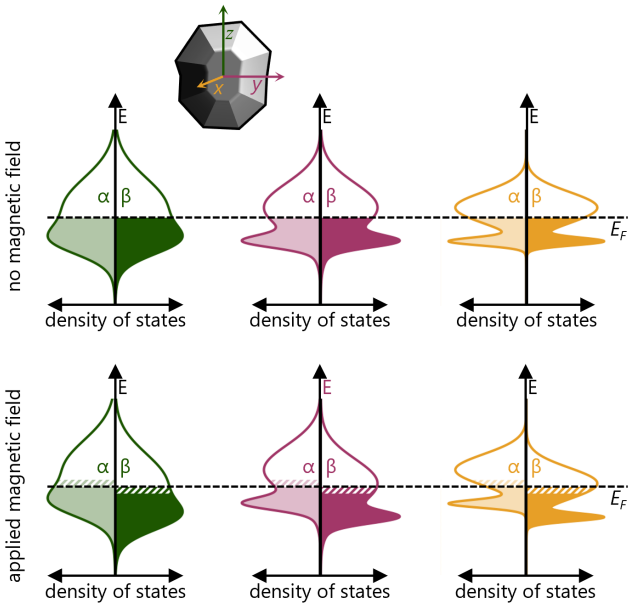

Figure 1: A nanoparticle that is asymmetric in shape should naturally be asymmetric with respect to its electronic properties. Specifically, the band structure should depend on the direction being considered. Shown here is the density of states associated with a projection of the electronic structure along a particular direction (yellow=x, magenta=y, green=z). Placing metallic particles in a magnetic field will produce Zeeman splitting of the α and β electron spin bands. Electrons will be transferred from the destabilized band to the stabilized band, producing a surplus of electrons at the Fermi energy (E_F, dashed black lines). Probing these unpaired electrons with electron paramagnetic resonance allows us to examine the nature of the electronic states at the E_F.

While strong motivation is needed, there is often not sufficient evidence that morphology matters for the electronic behaviors of small particles. At present, electronic spectroscopy (including plasmon spectroscopy) is the most common means of characterizing the electronic properties of metallic systems. However, owing to the broadness of electronic bands, the effects of morphological asymmetry are often unresolved by this technique.

Nevertheless, because the properties of particles lie farther from the bulk-scale limit as particle size decreases, the electronic structure (*e.g.*, band structure, Figure 1) of small particles, and the behaviors that this structure gives rise to, should be *more* responsive to changes in morphology than larger particles.[28] Small particles are also attractive candidates for use in commercial applications, as they provide more efficient use of metals, in terms of nanoparticles per mass. The same reasoning applies when attempting to maximize active surface area of metals, which is a critical concern in catalysis. Thus, small particles provide a largely untapped opportunity for strong tuning of the electronic properties that underlie their exciting applications, particularly for particles that are commercially desirable.

There are, of course, examples in which morphology plays a significant role in small metal-based systems. Atomically precise metal clusters demonstrate the power of small changes in morphology, where the electronic spectroscopy, electronic structure, and catalytic activity are all sensitive to changes as subtle as the movement of a single atom and the magnetic properties are sensitive to the ligands bound, as well as the crystallinity and charge of the cluster.[29–35] Indeed, even changes in morphology alone can be sufficient to drive molecule-to-metal transitions.[36] Yet, although morphological control of clusters is powerful, the majority of these clusters are not metallic, and so do not possess the same desirable properties as small metallic particles.

Within the world of small *metallic* nanoparticles, there are some examples of shape control, such as small cubes and other polyhedra for platinum.[37,38] Although such examples are known, the dominant terminology for small particles in the literature remains 'spheroidal'—reflecting a lack of specific knowledge of the morphology and its effects on electronic properties. Taking a cue from the realm of larger particles, determining the morphological effects directly for small nanoparticle systems would allow us to understand and tune their metallic behaviors. The first step along this path is developing a tool for measuring the impact of morphology on electronic structure and behavior.

Herein, we demonstrate such a measurement for a series of nanoparticles built from

copper, silver, palladium, iridium, gold, and platinum using electron spin resonance (ESR) spectroscopy. We develop a model that quantitatively connects morphological asymmetry with the ESR spectra. We then show that this morphology-based model developed for ESR spectra can be successfully applied to plasmon spectra of the silver particles. In total, this work suggests real and meaningful dependencies on morphology and suggests control of morphology as a useful tool for the myriad of applications based on electronic behaviors of small metallic particles.

Results and discussion

Nanoparticle Synthesis

Details of the synthesis for each nanoparticle system are provided in the materials and methods section. With the exception of the platinum species, the thiolate-protected particles could be produced directly from the metal salt *via* a process resembling the two-phase Brust-Schiffrin synthesis.[39] In the case of platinum, first amine-protected particles were synthesized, followed by a ligand-exchange with dodecanethiol. For all particles, once the thiolate species was present, it was purified *via* precipitation from organic solvent using either methanol or ethanol as the anti-solvent. The precipitates were then washed and collected for physical characterization and spectroscopy.

Physical characterization

The size and shape of our particles were determined using TEM. Figure 2 shows exemplar electron micrographs for each particle, as well as histograms of the sizes attained from analysis of the TEM images. The data shown here is for the longest chord that could be drawn within each particle, and which we then call the 'diameter.' Also shown are fits of log-normal distributions to these particles as well as box and whisker plots of the distributions. The fits were obtained from an in-house Python script, that bins the data and fits a log-normal distribution to this binned data using least squares. A complete description of the program can be found in the SI. Also reported in this figure are the geometric means (μ)

and standard deviations (σ) attained from the log-normal fits, as well as the average aspect ratio (AR), and the standard deviation in this measured aspect ratio (σ_{AR}).

We find that all of our particles have a geometric mean diameter of less than 5 nm, and a geometric standard deviation of less than 1.5 nm. The most tightly dispersed particles are the Ir particles, while the most widely dispersed particles are the Ag particles.

From the TEM micrographs shown in Figure 2, it can be seen that our particles almost exclusively fall into the 'spheroidal' category. This category is often invoked when particles do not have a definite shape, such as square, octahedron, bars, oblong, *etc.* Though the TEMs show obvious asymmetries in some particles, the nature of the asymmetries are not regular enough that one could classify the population with a definite shape. For instance, the Pt particles have occurrences that might be called triangular, but such particles are relatively rare within a larger population of spheroids. Nonetheless, we can at least provide an aspect ratio (AR) for the particles, by dividing the largest dimension for each particle in the TEM by the smallest dimension. Though this is not as well defined as it would be in the case of rods, it does provide a rough estimate of the asymmetry of the particles. If we use this as a rough measure of the extent to which the particle morphology deviates from spherical (and likely cylindrical) symmetry, we can see that the magnitude of the average morphological asymmetry does not differ strongly between the particle populations that we have prepared.

Beyond the lack of a common nameable asymmetry, we also note that, for the majority of the particles, there is no obvious faceted structure. Regardless, it is acknowledged that, even when particles appear circular in the two-dimensional TEM image, they likely posses faceted surfaces that prevent true spherical geometry. Thus, even when morphological asymmetry is not clearly evident in TEM, the term 'spheroid' should be taken as implying lower than spherical symmetry.

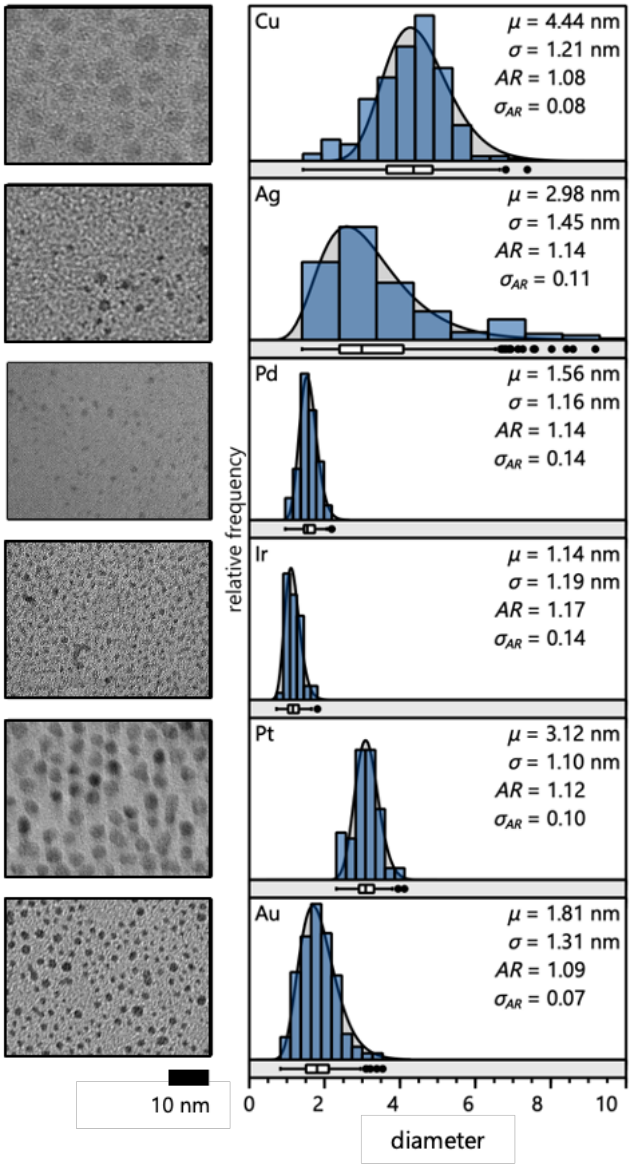

Figure 2: TEMs of the nanoparticles, as well as histograms of the particle diameters, box and whisker plots, and log-normal distributions fit to the histograms. The log-normal distributions are shown as the black lines with the gray fill. The box and whisker plots for each distribution are shown below the histograms. In the box and whisker plots, the box is the interquartile range (IQR), the whiskers are set at 1.5 times the IQR. Outliers are shown as circles, and the median value as the line in the box. In all cases, the 'diameter' is taken to be the longest chord that could be drawn within the particle. For each metal, we report the geometric mean (μ) and standard deviation (σ) associated with the log-normal distribution as well as the aspect ratio (AR) and standard deviation of the calculated aspect ratio (σ_{AR}).

Electron Spin Resonance

ESR spectra for our particles were acquired at 25 K, for dispersions in *n*-hexane. The spectra obtained are shown in Figure 3. Though we will be discussing the resonance position in terms of *g*-value, we plot the spectra *versus* the applied magnetic field, B. As discussed below, the simplest lineshape will be symmetric in terms of the applied field, and so plotting *versus* B aids in revealing the asymmetries present in our spectra. The resonance position, in terms of magnetic field, B_0, and the *g*-values are related by:

$$g = \frac{h\nu}{\beta B_0} \tag{1}$$

where h is Planck's constant, ν is the frequency of microwave radiation used in the instrument, β is the Bohr magneton.

Also shown in Figure 3 are fits (white lines) to the experimental data (blue lines) and the residuals of these fits (gray lines). The fitting is described in detail in the next two sections. In Figure 3, the experimental spectra have been background corrected, using a quadratic function obtained as a component of the model fit to the spectra. The uncorrected spectra, the background used for each spectrum, and a discussion of the selection of the quadratic background can be found in the SI (Figure S1).

Regarding the experimental ESR spectra, we note that four out of the six spectra are broad and apparently featureless. The exceptions to the apparent featurelessness are found in the Ir and Pt spectra, both of which have clear structure in the middle of the line shape. In general, the breadth of the spectrum increases as one moves from light to heavier metals. This is consistent with an expected increase in spin-orbit coupling (SOC) with increasing atomic number. Larger SOC should lead to faster spin relaxation, producing greater lifetime broadening of the ESR signals. The difference in spectral width does not, however, reflect the width of the particles' size distributions. Indeed, we observe that the broadest spectral widths are produced by the Ir particles, which also possessed the narrowest size distributions.

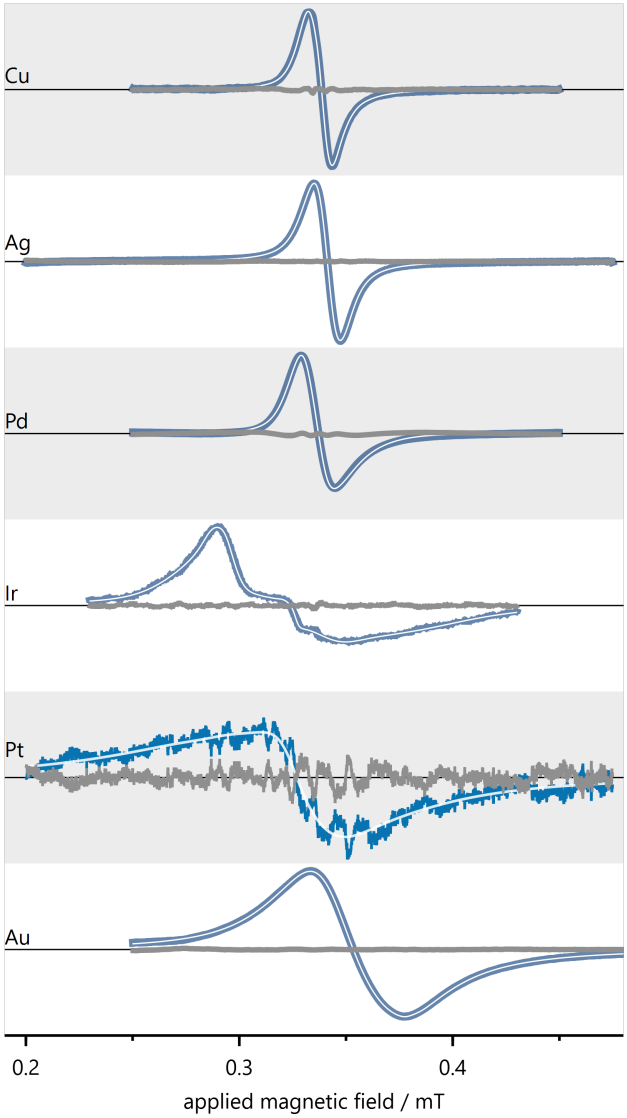

Figure 3: ESR spectra obtained for each of our particles. Experimental spectra are shown in blue and fits in white. The residuals of these fits are shown in gray. The fits are powder patterns built from pseudo-Voigt lineshapes. Parameters extracted from the fits are given in Table 1. Spectra shown here share the same x and y scales and have been adjusted by subtracting a quadratic background and then scaled so that the maximum absolute value of the fits is equal to 1. Raw spectra, and the background used to correct them, can be seen in the SI (Figure S1).

ESR spectroscopy probes the behavior of unpaired electrons, and the nature of the electronic states they occupy. Thus, before performing detailed analysis of the ESR spectra, it is worth considering the nature and origin of the unpaired spins probed in Figure 3. Although metals are often diamagnetic in the absence of an applied magnetic field, application of an external magnetic field can yield a spin polarization resulting in paramagnetism and an observable ESR signal.[40–44] This behavior, known as Pauli paramagnetism,[45] is a result of the continuum of electronic states found at the Fermi energy (E_F) for metals. Application of a magnetic field results in Zeeman splitting of the electronic bands (Figure 1) and, as a result, electrons are transferred from the band shifted to higher energy into the band shifted to lower energy, producing unpaired spin at the E_F. Thus, placing a metallic system in the magnetic field of an ESR instrument naturally produces unpaired spin in states near the E_F that can be used to probe the nature of these states.

Though Pauli paramagnetism is an expected behavior for metals, we must also consider other potential sources of unpaired spin. Our particles are relatively small and thus it is possible that they could display quantum size effects, and possess isolated paramagnetic behavior, rather than Pauli paramagnetism.[28] Quantum size effects occur when the particles become small enough in size that the spacing between electronic levels becomes large enough that the band picture is no longer valid. In this case, paramagnetism will be observed when we have an odd number of electrons in the particle. In addition, there exist reports of small nanoparticles displaying isolated paramagnetism, ferromagnetism, and even antiferromagnetism, often ascribed to so-called 'defect states' at the metal-ligand interface.[46] The model in Figure 1 was proposed with reference to Pauli paramagnetic behavior and, thus, if this model is to be valid for interpreting the ESR spectra we observe, it is necessary to decide if Pauli paramagnetism is the source of the unpaired spin we probe.

To this end, we measured the temperature dependent magnetic susceptability (χ) of our nanoparticles. For these measurements, we used a modified Evans NMR Method and the details of this approach, as well as the NMR measurements for each nanoparticle, are

presented in the SI (Figures S2 - S7). A summary of the results for all six nanoparticle systems, as well as for bulk palladium[47,48] are given in Figure 4.

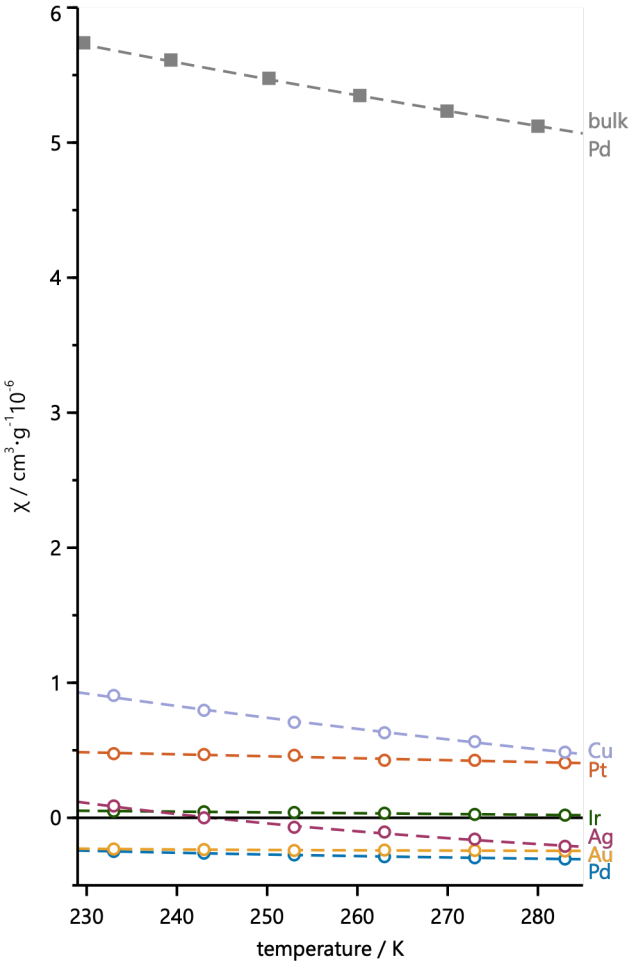

Figure 4: Magnetic susceptibility of the nanoparticles, as a function of temperature. Magnetic susceptibilities were measured using the Evans Method in NMR, as seen in the SI (Figures S2-S7). Also shown for reference is the magnetic susceptibility of bulk Pd.[49] Lines drawn through the data points are present merely to help guide the eye, and are not meant to imply a model equation.

The key to interpreting Figure 4 is the realization that the magnetic susceptibilities associated with Pauli paramagnetism behave differently from those associated with isolated paramagnetic centers. Here, we consider two key differences. First, Pauli paramagnetism is several orders of magnitude smaller than for isolated paramagnetism.[45] Indeed, for many real metals, which have large diamagnetic contributions from core electrons, the net magnetism can be diamagnetic—as is the case for several of our nanoparticle systems. For bulk transition

metals, palladium has the largest observed susceptibility,[47,48] and so provides an upper bound on what we might reasonably expect from particles displaying Pauli paramagnetism. Of course, it is worth realizing that Pd does not represent a 'pure' Pauli paramagnetic system, but one in which the magnetism that arises from band splitting (Pauli paramagnetism) undergoes Stoner enhancement. This enhancement is due to interaction with states that have large *d*-character, and the ability to interact with these states changes with temperature, which also explains the relatively large temperature dependence exhibited by Pd.[50] However, though this magnetism is not 'pure' Pauli paramagnetism, it is still intimately tied to the band structure of the metal and so should show dependencies on the morphology, as shown in Figure 1. Thus, even metals with behaviors that are similar to Pd will be sensitive to the morphological asymmetries under consideration.

As can be seen in Figure 4, all our particles have magnetic susceptibilities that lie well below that of bulk Pd, and so the degree of their magnetism is consistent with Pauli paramagnetism. Of course, this focus on the size of the magnetic susceptibility does not rule out extremely dilute amounts of isolated paramagnetic centers, and so we must also consider other behaviors that differentiate isolated paramagnetism from Pauli paramagnetism. This brings us to the measured temperature dependence.

Isolated paramagnetic centers follow the Curie-Weiss law[45] and show strong temperature dependence of their magnetic susceptibilities. On the other hand, Pauli paramagnetic systems have much weaker temperature dependence. Though they are often stated to be temperature independent,[45] this is only true for a free electron gas. Real metallic systems can display weak positive or negative temperature dependencies. Again it is palladium that serves as the upper limit, showing the strongest temperature dependence of bulk transition metals, due to modulation of the interaction with *d*-states in the metal.[47,48] And, again, we can see that all of the systems that we examine show weaker temperature dependence than bulk palladium. In the SI, the data shown in Figure 4 is replotted to make the relative strength of the temperature dependence more apparent (Figure S9).

From this analysis of Figure 4, we can see that the magnitude and temperature dependence of the magnetic susceptibilities of our particles are consistent with Pauli paramagnetism. Though we cannot rule out all possible, even exotic, sources of paramagnetism, we believe that the most likely reason that our metal nanoparticles display magnetism consistent with Pauli paramagnetism expected for metals is that, our metal systems are, in fact, behaving in a metallic fashion. Thus, below we interpret our data primarily with respect to the model shown in Figure 1.

Analysis of spectral asymmetry

The feature of the ESR spectra most salient to this report is that they are not symmetric. The simplest spectral shape for ESR is the derivative of a Voigt bandshape, which is symmetric. By symmetric, we mean that, when the spectrum is plotted *versus* the applied magnetic field, the most positive and negative features should be equal in magnitude, but opposite in sign when plotted *versus* the applied magnetic field, as well as equidistant from the point where the spectrum has zero intensity. The bottom spectrum of Figure 5a provides an example of this symmetric shape. A cursory examination of Figure 3 will show that many of our spectra strongly deviate from this symmetry. Perhaps this is most clear for the Ir, Pt, and Au spectra, which have asymmetries in both the *intensity* and *breadth*, but is also clear for Pd, which has clear asymmetries in intensity. We note that both Cu and Ag have similar, if far less pronounced, asymmetries.

Because ESR directly measures the ground state behavior of electrons in the metal particles, asymmetry in the lineshape is a reflection of asymmetries in electronic structure and behavior of these electrons. To characterize these asymmetries, we must first devise models that can account for them. When considering the nature of our samples, three primary candidates for explaining the asymmetry of the ESR spectra emerge. We now consider each of these.

The first potential source of asymmetry arises from the most commonly acknowledged asymmetry for small particles: size distribution. As shown in Figure 2, the distribution of

sizes follows a log-normal, which is intrinsically asymmetric. Thus, if the resonance position was expected to change with size, an asymmetrically distributed population will naturally produce a spectrum whose lineshape is asymmetric in both intensity and the width. Adding to this, one might expect an asymmetry in the dependence on size, in which the properties of particles asymptotically approach those of bulk metals as the particle size increases. As such, when a distribution of sizes are present, it is likely that they lead to an asymmetric distribution of electronic behaviors. The effects of these considerations are diagrammed in Figure 5b.

The second potential source of asymmetry that we consider arises from the metallic nature of the particles. It has long been known that metallic systems can produce strongly asymmetric ESR spectra, as a result of the high dielectric environment found within metals.[51] This high dielectric environment attenuates electromagnetic radiation as it passes through the sample (Figure 5c). This attenuation, in turn, produces a dispersive component of the spectrum. Combining dispersive with absorptive features produces a Dysonian lineshape[51] that is asymmetric with respect to both intensity and breadth of the spectrum. Specifically, as the contribution of the dispersive feature increases, the negative feature of the spectrum decreases in relative intensity, and also shifts farther from the zero crossing.

The final potential source of spectroscopic asymmetry is low morphological symmetry of the particles. Examining the TEM images shown in Figure 2, one can see that the particles, though mostly round, have clear asymmetries in shape. Thus, one might expect that the low symmetry of the particles would give rise to different g-values (resonance positions) along the cardinal directions, as shown in Figure 5d. The observation of three principal g-values due to low symmetry is an extremely common feature of molecules,[52] but we can also expect the same behavior for the metallic particles under consideration. As shown in Figure 1, low morphological symmetry will produce electronic structures that can be decomposed into three principal components. Because the g-value is determined by the nature of the ground states, the identity of nearby states, and the energy separation between

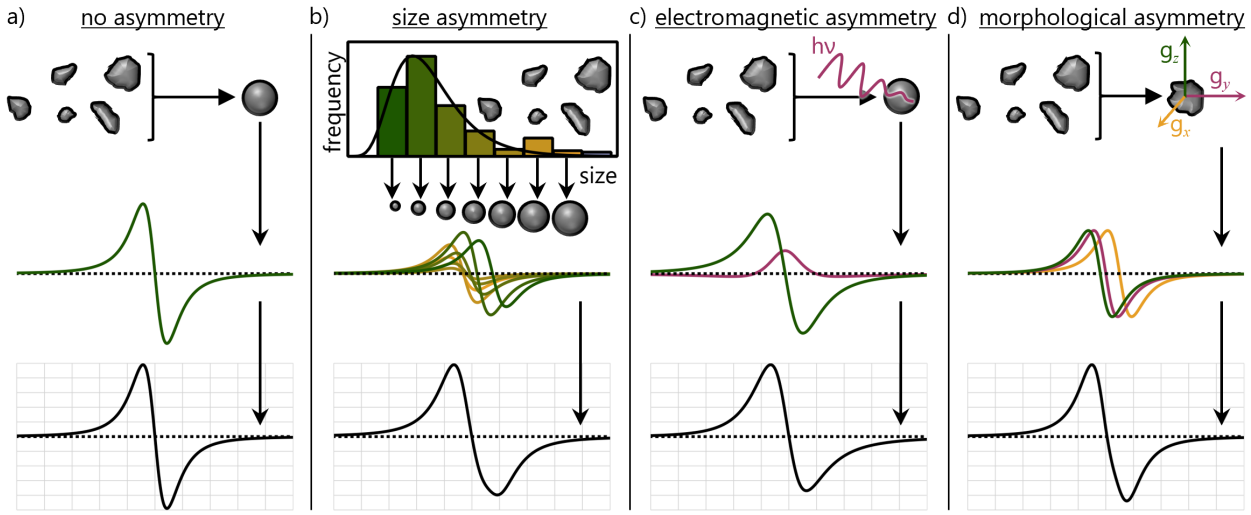

Figure 5: Illustrations of the different sources of spectral asymmetry, and how they are handled during fitting. A description of the mathematical models associated with these illustrations can be found in the SI. The top row of the figure depicts how particles might be approximated during fitting. The middle row demonstrates a sampling of spectra generated from this treatment. The bottom row presents the final spectra obtained, which is a sum of all of the individual spectra. For comparison, we include (a) the symmetric model, in which the nanoparticles are treated as a uniform population of spherical particles, and produces a symmetric ESR signal. (b) For size corrections, we treat individual particles as spheres and explicitly account for the distribution of particles sizes, each which produces a different ESR spectrum. Here, these are shown with their intensities weighted by their relative population. The final spectrum is a sum of these individual spectra. (c) In the Dysonian treatment, the size population is ignored and a single spherical particle is analyzed. The attenuation of the applied electromagnetic radiation within this particle produces both absorptive (green) and dispersive (purple) contributions to the final spectrum. (d) The simplest model for accounting for the morphological asymmetry is to treat the population by an 'average' particle, which has a single size, but retains asymmetry in x, y, and z. Such a particle will produce a large range of spectra, defined by the values associated with g_x, g_y, and g_z (spectra for these values shown), and the final spectrum is the sum of these spectra. In the fitting of our experimental spectra, we consider these models, and combinations of these models, which allows us to test for which of these potential sources of asymmetry are most likely to be the cause of the observed spectra asymmetry.

them, the differences in electronic structure shown in Figure 1 could be expected to result in different g-values along the cardinal directions. For particles frozen in solution, each particle could present a different orientation of these principal resonances to the applied field, and thereby a spectrum centered at a different position. Summing up over all of the orientations in the sample produces the observed spectra. This exact treatment is common for low symmetry molecules, where the result is termed a 'powder pattern.' Even when they are built from symmetric lineshapes, powder patterns can produce strongly asymmetric spectra if the principal resonances (oriented along x, y, and z) are unequally spaced or are associated with different linewidths.

We can summarize these three potential sources of spectra asymmetry as follows: in the first model, spectral asymmetry arises from asymmetry of the size distribution of the *population*. In the second model, spectral asymmetry arises from asymmetry in the applied *electromagnetic field*, *via* the action of the particles. In the third model, spectral asymmetry is a result of morphological asymmetry in the *individual particles.* Thus, each of these candidate models can potentially explain the observed spectral asymmetry, and each have a different underlying cause of this asymmetry. In order to distinguish between the veracity of each model in interpreting the data, we formed quantitative versions of the models and then fit them to our data. The metrics associated with the fits are then used to evaluate the dominant source of spectroscopic asymmetry, and provide insight into the electronic behavior of the particles.

Fitting of ESR spectra

We considered several models, which examined each of the above asymmetry sources individually, as well as combinations of them. For instance, we considered not only a basic Dysonian model (Figure 5c), which ascribes spectral asymmetry to asymmetry in electromagnetic field, and a basic powder pattern (Figure 5d), which ascribes asymmetry to the morphological asymmetry, but a combination of the two, whereby each particle was ascribed three principal Dysonian lineshapes. Such a model has two explanations for spectral asym-

metry and, in theory, both might be needed to account for our observed ESR line shapes.

Because so many models were considered, we do not present them all here. Instead, the full range of models we considered is presented in detail in the SI, and the fits of these models to the ESR spectra can be seen in Figure S2. Here, we simply outline the fitting procedure, the method of discriminating between fits, and the results of the model that provided the best fit.

All of the models were built from two components: one that accounted for potential physical origins of spectral asymmetry and one that accounted for the background response of the instrument. The former depended on the details of the physical model (Figure 5), while the latter was chosen to be a quadratic function for all of our models. Again, the mathematical details of these models, as well as a justification for the functional form of the background, is presented in the SI.

The final mathematical models at which we arrived had different total numbers of adjustable parameters. As a result, it is not possible to compare models using the sum of residuals. Instead, we used the Akaike Information Criterion (AIC) to discriminate between the fits to our data.[53–55] The value of this parameter for each model:spectrum pair that we fit, as well as a discussion of its interpretation, is presented in the SI. Here, we simply note that it is founded in information theory and the model that produces the most negative value for AIC is the model that is most likely to be correct.

Of the models that we considered, the most likely model was found to be a powder pattern built from pseudo-Voigt line shapes. It is the fits of this model to the experimental data that is shown as the white lines in Figure 3. This model considers *only* the morphological asymmetry and builds the powder pattern from a single model particle with 'average' morphological asymmetry, but which can exist at different frozen orientations. Thus, there are nine parameters associated with the particle: three principal g-values (g_x, g_y, g_z), as well as the Lorentzian full-width-at-half-maximum (FWHM_{L_x}, FWHM_{L_y}, FWHM_{L_z}) and Gaussian full-width-at-half-maximum (FWHM_{G_x}, FWHM_{G_y}, FWHM_{G_z}) associated with these princi-

pal g-values. The best fit values of these parameters, and their standard errors are given in Table 1. The standard errors are estimated from the fit, and are not obtained by repeated measurements on different samples. Given the run-to-run variance in populations for even well-controlled syntheses of nanoparticles, such repetition is difficult, though in the future it would be interesting to explore the effects of sample-to-sample variability. However, for this first communication, the primary result is that the most likely model is one that explicitly accounts for morphological asymmetry.

Table 1: The values, and their errors, of the parameters obtained by fitting the experimental ESR spectra to a powder pattern built from pseudo-Voigts. Reported are the resonance positions as g_x, g_y, and g_z, as well as the FWHM (in Hz) of the Lorentzian and Gaussian components associated with each g-value. The errors reported are the standard errors obtained as part of the fitting procedure.

Metal	g_x	g_y	g_z
Cu	1.9752 ± 0.0008	2.0232 ± 0.0003	2.0676 ± 0.0003
Ag	1.9600 ± 0.0002	1.9656 ± 0.0005	1.9900 ± 0.0002
Pd	1.9600 ± 0.0005	2.0259 ± 0.0007	2.0788 ± 0.0005
Ir	1.9515 ± 0.0029	2.0761 ± 0.0226	2.2869 ± 0.0012
Ir	1.7359 ± 0.0033	2.0646 ± 0.0010	2.3498 ± 0.0022
Au	1.8096 ± 0.0008	1.9530 ± 0.0008	2.0149 ± 0.0010
Pt	1.9808 ± 0.0062	2.0672 ± 0.0052	2.3496 ± 0.0022
	FWHM_{L_x} / 10^9 Hz	FWHM_{L_y} / 10^9 Hz	FWHM_{L_z} / 10^9 Hz
Cu	0.960 ± 0.020	0.288 ± 0.011	0.275 ± 0.006
Ag	1.568 ± 0.012	0.335 ± 0.005	0.315 ± 0.005
Pd	1.040 ± 0.068	0.354 ± 0.010	0.365 ± 0.010
Ir	1.700 ± 0.067	4.420 ± 0.555	0.363 ± 0.033
Ir	1.720 ± 0.174	0.165 ± 0.012	0.442 ± 0.015
Au	2.780 ± 0.018	1.530 ± 0.037	1.920 ± 0.023
Pt	2.530 ± 0.219	2.720 ± 0.466	5.590 ± 0.003
	FWHM_{G_x} / 10^9 Hz	FWHM_{G_y} / 10^9 Hz	FWHM_{G_z} / 10^9 Hz
Cu	0.266 ± 0.016	0.200 ± 0.007	0.403 ± 0.005
Ag	0.743 ± 0.008	0.420 ± 0.003	0.308 ± 0.003
Pd	1.140 ± 0.036	0.514 ± 0.014	0.359 ± 0.013
Ir	0.585 ± 0.030	0.199 ± 0.168	0.393 ± 0.013
Ir	1.760 ± 0.169	2.010 ± 0.073	1.110 ± 0.027
Au	1.340 ± 0.006	1.750 ± 0.007	0.540 ± 0.008
Pt	0.939 ± 0.003	0.400 ± 0.052	0.140 ± 0.058

We must also note that, though the pseudo-Voigt based powder pattern does provide the most likely model for five of our six particle systems, it is not the most likely model for the

palladium particles. For the palladium particles, it was found that a powder pattern based upon Dysonian lineshapes provided a more negative AIC. The SI presents the AIC for each model considered (Table S1). However, as this was the only particle for which this was true and because the Dysonian powder model also *explicitly* included morphological asymmetry, we felt that it was best to discuss all particles in terms of the pseudo-Voigt powder pattern and underlying morphological asymmetry.

A final note is required in regards to the fits shown in Figure 3 and the associated parameters given in Table 1. Examining the ESR spectra will show that both Ir and Pt particles gave rise to spectra with fine features. For the Ir, we were able to account for these features by including two sets of principal resonance values, giving rise to features of equal intensity. As shown in the SI (Figure S3), the AIC values showed the resulting fit to be preferred, and so we present these values here. At this point, we cannot conclude if this dual set of resonances is due to two different sub-populations of particles, or is an inherent property of the particles, such as could arise from twinning within individual particles.

In the case of Pt, the features are reminiscent of hyperfine splitting. However, we were unable to obtain improved fitting by including hyperfine splitting in our model. Even using the known pattern of Pt_{13} clusters[56] did not account for these features. A likely reason is that the spacing between features is not regular enough to allow for simple treatment. The signal from the platinum particles was, by far, the weakest (Figure S1) and so these apparent features may very well be noise. Because we could not account for the fine structure in the platinum ESR spectrum, we used the values extracted from the basic powder fit in this report and it is these parameters that we consider further.

Extracted g-values

The three principal g-values: g_x, g_y, and g_z obtained from our fits can be found in Table 1. In ESR, a related parameter is the g-shift, Δg, or the amount by which the g-value deviates from the free electron value of approximately 2.002319. This, in turn, is a measurement of the effects of SOC experienced by the electron involved in the spin transition, as it is through

the action of SOC that g-values depart from the free electron value.[28,45]

Accurate prediction of Δg is difficult, even for well-defined systems, as it depends upon the angular momentum of the ground state, excited states, and the energy gap between these states. For systems such as ours, where the morphology is ill-defined and so the precise electronic structure uncertain, reasonable prediction is currently impossible. Nevertheless, one might naïvely expect that, as the SOC of the individual metal atoms increases, so too would the magnitude of Δg.

To test this reasoning, we obtained estimated values of SOC constants of our metal atoms from literature values[57] and compared them to the absolute value of the observed Δg (Table 2). It should be noted that the SOC constants we used were obtained for isolated metal ions, rather than for neutral atoms in metals. Nevertheless, these values are expected to provide an indication of the relative trends in SOC constants for the atoms. Given that the SOC constants are for isolated atoms, they are also isotropic. For this reason we also chose to use the isotropic g-shifts for our particles, $\langle \Delta g \rangle$, which is obtained from the arithmetic mean of the g_x, g_y, and g_z values. Because it is the magnitude, not the sign, of Δg that depends on SOC, we also considered the absolute value of the isotropic g-shift, $| \langle \Delta g \rangle |$.

The correlation between the SOC constants and the observed $| \langle \Delta g \rangle |$ is shown in Figure 6. Given the rather tenuous connection between the SOC constants of isolated ions and that of our systems, the observed R^2 value of 0.789 is strikingly good. To be clear, the correlation is far from excellent, nevertheless, using the SOC as a loose proxy for our system, shows that is it not unreasonable to ascribe increasing $|\Delta g|$ to increasing SOC.

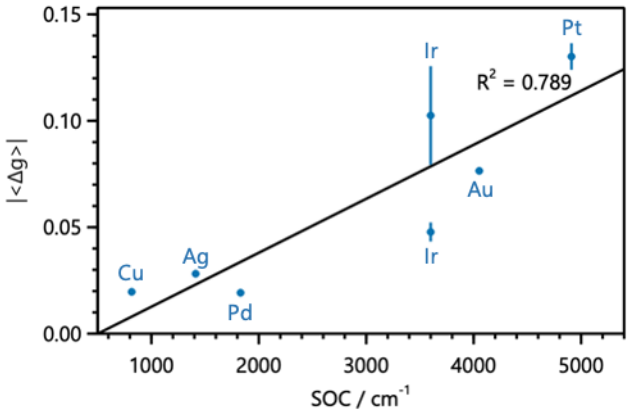

Figure 6: The absolute value of the g-shift, Δg, *versus* the spin-orbit coupling constants for an isolated metal ion. The black line was obtained by a least squares fit of a linear equation to this data. The error bars indicate the standard error obtained from the fit of the ESR spectra.

Table 2: Values of the SOC constants for the various metals, as well as parameters calculated from those in Table 1. Calculated parameters are the isotropic g-value ($\langle g \rangle$), sum of relaxation rates (τ_{exp}^{-1}), and the average standard deviations of the Gaussian contribution to the widths ($\langle FWHM_G \rangle$). The errors given are obtained by propagation of the errors in Table 1.

Metal	SOC / cm^{-1}	$\langle g \rangle$	τ_{exp}^{-1} / 10^9 s^{-1}	$< FWHM_G >$ / 10^9 Hz
Cu	817	2.0220 ± 0.0009	1.523 ± 0.024	0.290 ± 0.020
Ag	1412	1.9742 ± 0.0006	2.218 ± 0.014	0.490 ± 0.008
Pd	1830	2.0215 ± 0.0010	1.759 ± 0.069	0.671 ± 0.037
Ir	3600	2.1048 ± 0.0231	6.483 ± 0.560	0.392 ± 0.332
Ir	3600	2.0501 ± 0.0045	2.327 ± 0.175	1.627 ± 0.172
Au	4052	1.9258 ± 0.0015	6.230 ± 0.047	0.808 ± 0.038
Pt	4910	2.1325 ± 0.0346	10.084 ± 0.515	0.580 ± 0.216

Lorentzian contribution to linewidths

Though SOC is difficult to predict for our particles, the values of Δg are, to some extent, an *experimental* determination of this property. Thus, we might expect Δg to correlate well with other behaviors of the particles. The most obvious is the excited state decay rate (reflected in the Lorentzian widths), as increasing SOC facilitates the electron spin flip required for relaxation. Indeed, theory[28] predicts that the rate of relaxation (τ^{-1}, where τ is the excited state lifetime) is directly proportional to Δg^2. Given the small size of the particles, the mobility of metallic electrons, and the mean free path of electrons in metals, we expect that the electronic wavefunction should explore the full particle during its excited state lifetime (nanoseconds). In addition, we expect that there could be scattering events that change the momentum (k-state) of the electron without causing relaxation. Both of these mean that the excited electronic state can continue to evolve over its lifetime such that all g-values could be implicated in the relaxation of the electron. Thus, we judge that the average g-value, $\langle \Delta g \rangle$, is the appropriate parameter to use. If the relaxation mechanism for any given electron can be sensitive to the different g-values, then the observed relaxation rate should be given by the sum of the rates along x, y, and z. In other words the expected rate, τ_{exp}^{-1}, is expressed as:

$$\tau_{exp}^{-1} = \tau_x^{-1} + \tau_y^{-1} + \tau_z^{-1} \tag{2}$$

where the values of τ_x^{-1}, τ_y^{-1}, and τ_z^{-1} can be obtained from the FWHM values of the Lorentzian components of the pseudo-Voigt (Table 1). The values we obtain for τ_{exp}^{-1} are given in Table 2.

In addition to the above physical reasoning, there is a spectroscopic reason to consider the combined relaxation rate. The three principal components of the ESR spectra are not well-resolved, and so the exact values of the Lorentzian widths along x, y, and z do not carry as much meaning as they would if these components were spectroscopically well-resolved. Instead, it is the overall width that carries the most clear meaning, which is again tied to the idea of an average relaxation rate, as approximated in Equation 2.

Figure 7 plots τ_{exp}^{-1} *versus* $\langle \Delta g \rangle^2$, and shows a good correlation between these parameters ($R^2 = 0.949$). Thus, it seems that the g-values we extract from our model are physically meaningful, and provide some prediction of the behavior of the metallic electrons.

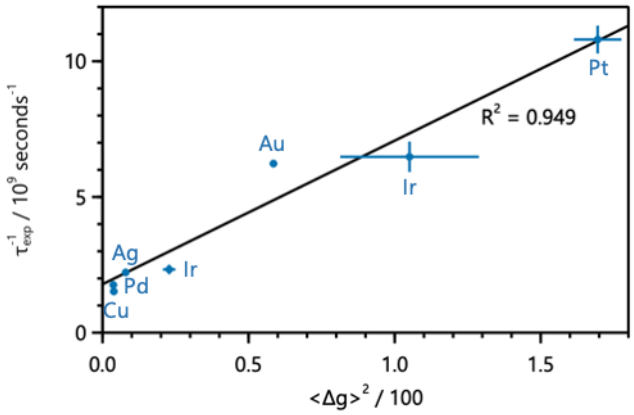

Figure 7: A plot of τ_{exp}^{-1} (Equation 2) *versus* the square of the average g-shift, $\langle \Delta g \rangle^2$. The error bars indicate the standard error obtained from the fit of the ESR spectra. As both the dependent and independent variables have errors, the black line was obtained using orthogonal distance regression to fit a linear equation to the data.

Gaussian contribution to linewidths

Gaussian linewidths are also obtained from our fits. These report on the inhomogeneous broadening of the signal. There are numerous possible sources for this broadening. One arises from the particles themselves, which have a distribution of particle sizes. Moreover, we expect that there should be a distribution of shapes, surface coverage by ligand, and possibly even different surface bound species. For instance, thiols are known to bind to gold as single species, staples, and double staples, to name a few, and all of these could be present to differing degrees from particle to particle.[58] In addition to these asymmetries intrinsic to the particles, the environments around the particles in the frozen solution are unlikely to be homogeneous. All of these considerations could make contributions to the spectral width.

Given the number of possible contributors, it is perhaps unsurprising that we had difficulty finding parameters of the sample that showed good correlation with the Gaussian widths. The best correlation we were able to identify involved the diameter of the particle,

with the Gaussian broadening decreasing with increasing particle diameter, as shown in Figure 8. In this Figure, the solid line is the result of fitting to a d^{-3} dependence, where d is the particle diameter, reflecting that the values observed are expected to approach a final value as the particle size approaches the bulk and that this approach should depend on the number of atoms, which grows as the cube of the diameter.

This behavior makes sense if one considers that as particles become larger and larger, it will take larger changes in the shape to create similar morphological asymmetry. In addition, as the particles grow in size, their electronic properties will approach the bulk values. Thus, changes in shape also become less meaningful. Finally, as the particle size increases, the importance of inhomogeneities at the surface, such as in surface chemistry and environment, will exert a decreased influence over the particle's properties. Thus, we should expect that inhomogeneous broadening will be largest for the smallest particles, which is generally what we observe.

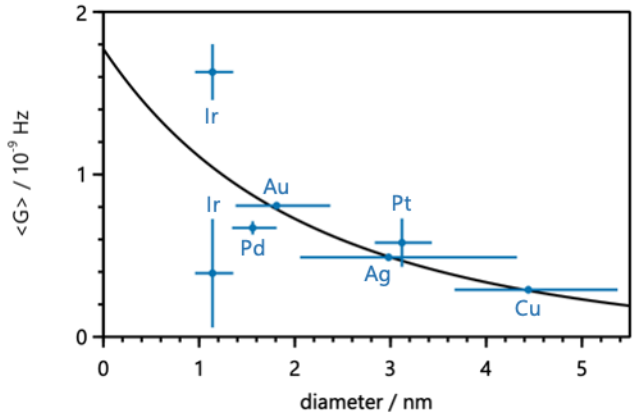

Figure 8: A plot of the average of the Gaussian full-width-at-half-maximum, $\langle FWHM_G \rangle$ *versus* the diameter of the particles, d. The vertical error bars indicate the standard error obtained from the fit of the ESR spectra. The horizontal error bars indicate ± 1 standard deviation about the mean of the lognormal shown in Figure 2. The fit line was obtained using orthogonal distance regression to fit an r^{-3} dependence to the data. Due to the non-linear nature of the fit, no R^2 is provided.

Electronic spectra

The above analysis of ESR spectra revealed asymmetry in the electronic properties for the electrons near the E_F. These electrons are also involved in the plasmon resonance of metallic particles. As such, asymmetries in the properties of the electrons at the E_F might be expected to result in asymmetries in the plasmon spectra associated with the particles.

Of the metals we examined, the only species that produced a plasmon that was simultaneously strong enough for analysis and unobscured by the solvent were the silver particles. Though gold particles of the size we employed do have a plasmon, it is extremely damped, and not pronounced enough for the analysis that follows. Figure 9 shows the UV-vis spectrum in the region of the plasmon for the silver particles as dispersions in n-hexane at room temperature. The full range of the data collected can be seen in the SI (Figure S4).

The spectrum in Figure 9 shows the apparently featureless band typical for plasmons of spheroidal particles. A typical treatment of this plasmon resonance would be to fit the spectral profile using a single Gaussian function, combined with an exponential decay. The Gaussian captures the plasmon resonance, while the exponential decay accounts for the shoulders of nearby electronic bands, as well as the background scattering and absorbance of the electrons in the metal. Figure 9a shows the results of such a fit to our spectrum. In this Figure, the fit is shown as a white line, and the residuals as grey lines. The exponential decay is shown in light purple, and the Gaussian in dark purple.

Although the fit of this spectrum does have regions where the fit and the experimental spectra deviate (notably, near 600 nm), this fit is one that would often be considered sufficiently good for extracting spectral parameters. However, in light of the ESR results, we wondered if the plasmon could be better reproduced by accounting for the morphological asymmetry of the particles, and the electronic asymmetry it produces. As was the case for the ESR spectra, we considered a number of such models, and these are described in detail in the SI. Here, we show the results of two of these models.

In Figure 9b, we show the results of fitting the spectrum using three Gaussian profiles,

plus an exponential decay. The exponential decay is shown in light purple, while the Gaussians are drawn in green, dark purple, and orange. We also considered models involving between one and three Gaussian bands and, as can be seen in the SI, the model with three Gaussian bands produced the most likely fit, from the perspective of the AIC (Figure S5).

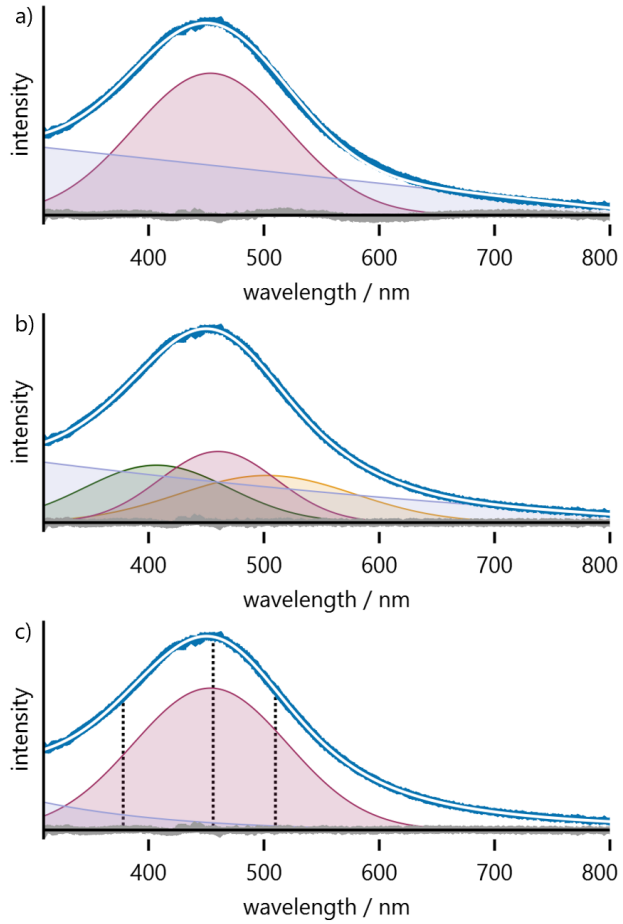

Figure 9: Comparison of fits from different models (white lines) to the experimental UV-visible spectrum (blue lines) of the silver particles, in the region of the surface plasmon resonance. The residuals of the fits are shown as the grey lines. In all models, the background was treated by an exponential decay, shown in light purple. To this decay, functions intended to reproduce the plasmon resonance band are added. (a) A fit of a single Gaussian (dark purple) to the experimental data. (b) A fit to three Gaussians (dark green, dark purple, and orange) to the experimental data. (c) A fit of a powder pattern constructed from Lorentzians (dark purple) to the experimental data. For the powder fit, the position of the principal resonances (λ_x, λ_y, and λ_z) are indicated by the dotted vertical lines.

In this treatment, we assume that the three Gaussian bands represent three different transitions. In other words, there are three principal plasmon resonances (just as there are

three principal g-values) and these resonances are broadened to produce the Gaussian bands.

The SI shows that Gaussian bands are preferred over both Lorentzian and pseudo-Voigt bandshapes. This is a significant result, because the lifetime of plasmons is extremely short and the particles are in liquid solution. The short lifetime should produce significant homogeneous broadening, with an associated Lorentzian linewidth, while the liquid state should allow for motional narrowing that reduces the importance of the Gaussian contribution. Though particles translate and tumble slowly, the solvent and the ligands both have faster motion, and solvent motion is well known to affect electronic absorption features.[59] Both of these suggest that Gaussian broadening should not dominate. Thus, the dominance of the Gaussian shape suggests a different model might be appropriate: one built upon the same powder pattern used to reproduce the ESR spectra.

The rational for introducing powder patterns to the fitting of UV-vis spectra comes from the extremely short lifetime of the excited plasmon, which is on the order of tens to hundreds of femtoseconds.[60] Given the mass of our particles, their rotational lifetimes are much longer than the plasmon lifetime. The result of this difference in lifetimes is that, from the perspective of the excited plasmon, the particles are frozen in place, and will present a distribution of orientations with respect to the electromagnetic radiation used to drive the plasmon resonance. This is analogous to the situation that gives rise to the powder pattern observed in ESR and, if true, then a powder pattern should produce a fit to the experimental data that is of similar quality to that given by the use of three Gaussians (Figure 9b).

To this end, we modified our Python code for ESR to allow fitting of a powder pattern to the experimental plasmon spectrum. A description of this model is provided in the SI. Figure 9c shows the result of these fits, where the exponential decay is again shown as light purple, while the powder pattern is shown as dark purple. This fit used Lorentzian lineshapes for the individual resonances. The positions of the principal resonances were $\lambda_x = 510.0 \pm 1.6$ nm, $\lambda_y = 455.7 \pm 1.1$ nm and $\lambda_z = 378.4 \pm 1.1$ nm, while the FWHM associated with each resonance were $FWHM_x = 157.8 \pm 2.8$ nm, $FWHM_y = 138.1 \pm 3.2$

nm, and $FWHM_z = 154.5 \pm 3.1$ nm. The position of the principal resonances is also shown in Figure 9c. The arithmetic value of the plasmon resonances is 448.0 ± 2.2 nm, which lies in the normal range of values for spheroidal silver particles.

It is important to note that we found that the use of the powder pattern built from Lorentzian lineshapes produced a fit of similar quality to that of given by three Gaussian bands. In other words, if one simply assumes three principal resonances and ascribes to them fully homogeneously broadened bands, this nearly reproduces the quality of the fit assuming heterogeneously broadened bands. This is a striking result, because the use of purely homogenously broadened bands for the powder pattern means that we are ignoring the broadening effects of the size distributions shown in Figure 2. In other words, as was the case for the ESR, we find that morphological effects are more important for explaining our spectra, than distributions of size.

When considering the values of the parameters extracted from the powder fit to the plasmon, it is also important to note that, while λ_x, λ_y and λ_z are widely spaced, they are associated with the principal components of a *powder pattern*. Thus, the x and z resonance positions are found approximately at the point of steepest slope in the band, while the y resonance is found approximately at the band maximum.

Finally, though we only have a pair of g-values and plasmon values, it is tempting to see if they have any connection to each other. To test this, we can simply plot the observed g_x, g_y, and g_z values obtained from the ESR powder fits *versus* the energies associated with the plasmonic resonances. Doing so yields the plot shown in Figure 10. The correlation between these values is quite good, giving an R^2 of 0.974. However, it should be stressed that we only have three data points at this time, and validation of this connection, as well as development of a theoretical understanding of the connection between them, will require further research. For instance is is likely that the larger sized particles in our distribution contribute more strongly to the plasmonic signal, while the ESR could be argued to be biased towards small particles. However, in both cases, we find that explicit consideration

of morphological asymmetry yields better analysis of the electronic effects. In addition, it is satisfying that the values obtained from the same model for these different electronic phenomena show a good correlation.

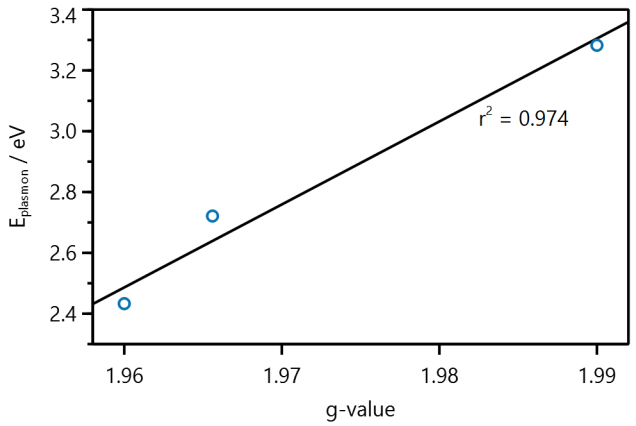

Figure 10: Energy of plasmon resonance *versus* g-value for silver particles. The energy of the plasmon resonances was obtained from powder fitting of the plasmon spectrum (Figure 9c). The g-values were obtained from a powder fitting of the ESR spectrum (Figure 3). The result of fitting a linear equation to this data is shown as the black line, using an orthogonal distance regression.

Conclusions

The key insight of this paper is that small spheroidal metallic nanoparticles possess electronic asymmetries that can be ascribed to morphological asymmetries in the particles, and that these morphological considerations can be more important than size distributions in accounting for electronic asymmetries. Indeed, for the particles we examined, we were able to completely ignore the size distribution in our treatments of the spectra. While this result should not be taken as evidence that size does not matter, we believe that it does indicate that morphology is more important, when dealing with particles that are as tightly distributed as the ones we have used. It also suggests that understanding how to control morphology for small metallic particles will carry more impact in their use than understanding how to more tightly control their size.

To reach this conclusion, we have shown clear demonstration of the electronic asymmetries using ESR spectroscopy, which provides sufficient resolution to make the electronic asym-

metries readily apparent as asymmetric spectra. We have also shown that these asymmetric spectra are best accounted for using standard ESR treatments that explicitly acknowledge morphological asymmetry.

We have also shown that the electronic asymmetries revealed by ESR can be invoked to explain other electronic behaviors, such as the plasmon resonance. Though plasmon resonances of spheroidal particles are often considered featureless, and treated as symmetric bands, we show that one can leverage the same model used to account for the effects of morphology in ESR to produce an improved fit of the experimental plasmon spectra of our particles.

While more work is needed to clarify the physical relationship between parameters extracted from ESR and plasmon measurements, this work provides evidence that morphology matters for spheroidal particles, and that it matters for behaviors that are widely used, such as the plasmon. To the extent that other behaviors, such as plasmonic coupling and catalysis, are tied to electronic structure, morphological asymmetry will likely matter for them as well. For instance, orientation of these particles could improve generation of plasmonic hot spots, and the need to have both fine-tuned spacing and orientation could account for the relative paucity of these hot spots in films constructed from spheroidal particles.

Materials and Methods

Materials Nanopure water used as 18.2M$\Omega \cdot cm^{-1}$ purity, obtained from an in-house Labconco WaterPro BT water purification system. Copper (II) chloride dihydrate (99.999% Cu) was purchased from Strem Chemicals. Tetraoctylammonium bromide (TOAB, 98+%), sodium borohydride (99%, VenPure SF powder), dihydrogen hexachloroplatinate (IV) hexahydrate (99.9%), potassium hexachloroiridate (IV) (min. 39% Ir), sodium thiosulfate (anhydrous, 99%), and chloroauric acid trihydrate (99.999%) were purchased from Alfa Aesar. Silver nitrate (99.9999%) potassium tetrachloropalladate (98%), 1-dodecanethiol (98+%) and dodecylamine (98%) were obtained from Sigma-Aldrich. 1-bromododecane (98%) was obtained from Acros Organics. Potassium bromide (>99.0%, ReagentPlus) was obtained from Honeywell. Solvents were obtained from Fisher Chemical. All reagents were used as received without further purification.

Preparation of nanoparticles

Copper dodecanethiolate-protected nanoparticles

Copper nanoparticles (CuNPs) were synthesized according to a modified Brust-Schiffrin synthesis.[61] $CuCl_2 \cdot 2H_2O$ (0.158g, 0.925 mmol) was dissolved in 30 mL of water in the presence of KBr (7.18g, 0.0604 mmol) to convert Cu^{2+} to $CuBr_4^{2-}$ due to the poor phase transfer efficiency of the copper cation. While vigorously stirring, TOAB (2.12g, 3.88 mmol) dissolved in 80 mL toluene was added to the reaction. After transfer, the clear, colorless aqueous layer was removed from the deep purple organic layer. The toluene solution was stirred under nitrogen for ca. 30 minutes. 1-dodecanethiol (1.08mL, 4.50 mmol) was added to the solution to produce a clear, colorless solution. A freshly prepared solution of $NaBH_4$ (0.4M, 25mL) was added to the vigorously stirring solution and stirred under nitrogen for 3 hours prior to purification. Once separate from the aqueous phase, the volume of the organic phase was reduced to ca. 10 mL using a rotary evaporator. Following this ethanol (200mL) was added to the dispersion and the mixture placed in the freezer overnight, during which time the par-

ticles formed a precipitate. The CuNPs were collected the following day over a fine-fritted filter.

Silver dodecanethiolate-protected nanoparticles

Silver nanoparticles (AgNPs) were synthesized according to a modified Brust-Schiffrin synthesis. TOAB (1.64g, 3.00 mmol) was dissolved in 100 mL of toluene and mixed with a 50mL aqueous solution of $AgNO_3$ (0.184g, 1.09 mmol). While stirring, KBr (1.38g, 11.6 mmol) was added to the reaction to promote the formation of $[AgBr_2]^-$ for phase transfer to the organic phase. Then, the two-phase reaction mixture was heated to 80°C for 30 minutes to facilitate the phase transfer of the metal ion precursor to the organic phase. Both the aqueous and organic phase became clear and colorless upon transfer of Ag^+. The aqueous layer was removed after 30 minutes, and the organic phase was allowed to cool to room temperature. A freshly prepared solution of cold $NaBH_4$ (1.0M, 10.0mL) was added to the vigorously stirring solution. The organic phase became a light gold color. Almost immediately, 1-dodecanethiol (360μL, 1.50 mmol) dissolved in 5-10 mL of toluene was quickly injected into the reaction flask and allowed to stir for 4 hours, prior to purification. The dark red-brown organic phase was separated from the aqueous layer and washed with nanopure water (10mL, 3x) prior to being concentrated to ca. 50mL with a rotary evaporator. The particles were precipitated with ethanol (ca. 100mL) in a freezer overnight, and collected *via* centrifugation at 10,000rpm for 10-15 minutes.

Palladium dodecanethiolate-protected nanoparticles Palladium NPs (PdNPs) were synthesized according to a modified literature procedure.[62] Briefly, K_2PdCl_4 (0.620g, 1.89 mmol) was added to 62.7mL of nanopure water. A 167mL solution of TOAB (4.57g, 8.36 mmol) in toluene was added and allowed to stir for ca. 10 minutes. 1-dodecanethiol (420 μL, 1.75 mmol) was added to the organic phase. Almost immediately, a freshly prepared solution of cold $NaBH_4$ (0.4M, 51.7mL) was added to the vigorously stirring solution, becoming a black color. This was allowed to stir for 6 hours, prior to purification. The organic phase was washed with nanopure water (10mL, 3x), and concentrated using a rotary evaporator. The

particles were precipitated using ethanol (200mL) overnight in the freezer. The particles were collected the following day by centrifugation at 10,000rpm for 30 minutes.

Platinum dodecanethiolate-protected nanoparticles

Platinum nanoparticles (PtNPs) were synthesized using a modified literature procedure.[63] Briefly, $H_2PtCl_6{\cdot}6H_2O$ (0.312g, 0.6mmol) was added to a round-bottom flask and dissolved in 30mL nanopure water. A solution of TOAB (0.984g, 1.8mmol) in 60mL toluene was prepared and added to the stirring hexachloroplatinic acid solution. Over the course of the phase transfer, the aqueous layer became colorless, while the organic layer turned orange. The mixture was stirred two hours to ensure complete transfer of hexachloroplatinate to the organic phase.

Dodecylamine (2.44g, 13.2mmol) was then added, and after five minutes of stirring, followed by a dropwise addition of a 20mL solution of aqueous $NaBH_4$ (0.5M, 20mL). The mixture gradually turned dark brown, and was left to stir for two hours. The organic phase was separated and 400mL isopropanol was added to precipitate the dodecylamine-protected PtNPs. The mixture was stored in a freezer overnight, centrifuged at 10,000rpm for 15 minutes, and the non-solvent decanted from the pelleted PtNPs. The nanoparticles may be redispersed in a variety of low-polarity organic solvents, such as $n-$hexane or THF.

Dodecylamine was replaced with dodecanethiol on the surface through a ligand exchange process. As an example, 100mg PtNPs was dissolved in 50mL THF, and dodecanethiol (0.347mmol) added. The solution was stirred overnight, precipitated and collected as above to obtain dodecanethiolate-protected PtNPs.

Iridium dodecanethiolate-protected nanoparticles

Iridium nanoparticles (IrNPs) were synthesized following a literature procedure.[64] K_2IrCl_6 (1.09g, 0.4mmol) was added to a round-bottom flask and dissolved in 30mL nanopure water. A solution of TOAB (0.984g, 1.8mmol) in 60mL toluene was added to the stirring $IrCl_6^{4-}$ solution. The mixture was stirred until the aqueous layer became colorless and the organic layer became orange to ensure complete transfer of hexachloroiridate to the organic phase, which

was then separated from the aqueous layer. Thiols react with hexachloroiridate to form the complex $Ir(SR)_3$ which resists reduction by $NaBH_4$. Instead, sodium S-dodecylthiosulfate was prepared by alkylation of sodium thiosulfate with bromododecane, and used as a thiol precursor. Sodium S-dodecylthiosulfate (0.80 mmol) and an additional 2.0 mmol of TOAB was added with 10mL 40% aqueous methanol. The mixture was then heated to 60°C for 15 minutes, after which $NaBH_4$ (8.0mL, 1.0M) was quickly injected into the reaction mixture. The mixture was stirred for an hour and cooled to room temperature, after which the organic layer was separated, washed with water and concentrated on a rotary evaporator. Methanol (300mL) was added to precipitate the particles, which were then collected by centrifugation. The resulting nanoparticles can be redispersed in a variety of low-polarity organic solvents.

Gold dodecanethiolate-protected nanoparticles

The two-phase synthesis of gold nanoparticles (AuNPs) at room temperature used by our laboratory has been previously described.[41] Briefly, $HAuCl_4.3H_2O$ (35 mg, 0.900 mmol) was dissolved in 25 mL of DI water. A 60 mL solution of TOAB (2.19 g, 4.00 mmol) in toluene was added to the aqueous $AuCl_4^-$ solution, and the two-phase mixture was vigorously stirred for ca. 10 minutes. Then, 2.81 mmol of the alkanethiol ligand was added to the organic phase while stirring. Immediately following the addition of the ligand, 25 mL of an aqueous 0.1 M $NaBH_4$ solution was added dropwise to produce AuNPs. The reaction was allowed to stir for 3 hours, prior to purification. The AuNPs were precipitated with methanol (200 mL), placed into a freezer overnight, and collected the following day over a fine-fritted filter.

Characterization. Transmission electron microscopy was performed on an FEI Tecnai G20 20 XTWIN LaB6 at an accelerating voltage of 200kV. Samples were prepared by drop-casting dilute nanoparticle dispersions in *n*-hexane onto carbon-coated copper grids (200 mesh, Electron Microscopy Sciences). Nanoparticle sizes (at least 200 for each metal) were measured using ImageJ software (National Institutes of Health). NMR spectra were obtained using a Bruker Avance NEO Nanobay 400 with all chemical shifts reported in ppm. Samples were prepared for NMR by suspending a known mass of particles in a known volume

of n-hexane (THF for IrNPs) and transferring to a 530μL coaxial insert, with a stem length of 50mm. The coaxial insert was placed in a 5mm O.D. thin-walled precision NMR tube containing $CDCl_3$. UV-vis spectra were acquired on an Ocean Optics USB2000+ spectrometer in n-hexane. A quartz cuvette with a 1 cm path length was used for all measurements. Continuous-Wave (CW) CESR measurements were performed using a Freiburg Instruments MS-5000X X-band spectrometer augmented with a ER 4112-HV Oxford Instruments variable temperature helium flow cryostat to achieve 25K. All measurements were performed using 100 mW of microwave power. The saturated solutions of NPs used for ESR were prepared with n-hexane, degassed by freeze-pump-thaw, and sealed with paraffin wax tape in clear fused quartz tubes with 4mm O.D./3mm I.D.

Acknowledgement

The Authors thank Prof. Alexey Silakov for many helpful discussions regarding the fitting of power patterns, and for ESR spectra against which the Python code was validated. The authors acknowledge the NSF (CHE-1609572 and CHE-2003609) for financial support of this work.

Supporting Information Available

Description of all fitting procedures, uncorrected ESR spectra, discussion of AIC and the values associated with the fitting, full UV-vis spectrum for the silver particles. This material is available free of charge via the Internet at `http://pubs.acs.org/`.

References

1. Bardhan, I.; Lal, S.; Joshi, A.; Halas, N. J. Theranostic Nanoschells: From Probe Design to Imaging and Treatment of Cancer. *Accounts of Chemical Research* **2011**, *44*, 936–946.

2. Huan, X.; Jain, P. K.; El-Sayed, I. H.; El-Sayed, M. A. Plasmonic Photothermal Therapy (PPTT) Using Gold Nanoparticles. *Lasers in Medical Science* **2007**, *23*, 217–228.

3. Dreaden, E. C.; Alkilany, A. M.; Huang, X.; Murphy, C. J.; El-Sayed, M. A. The Golden Age: Gold Nanoparticles for Biomedicine. *Chemical Society Reviews* **2012**, *41*, 2740–2279.

4. Stawart, M. E.; Anderton, C. R.; Thompson, L. B.; Maria, J.; Gray, A. K.; Rogers, J. A.; Nuzzo, R. G. Nanostructured Plasmonic Sensors. *Chemical Reviews* **2008**, *108*, 494–521.

5. Anker, J. N.; Hall, W. P.; Lyandres, O.; Shah, N. C.; Zhao, J.; Duyne, R. P. V. Biosensing with Plasmonic Nanosensors. *Nature Materials* **2008**, *7*, 442–453.

6. Willets, K. A.; Duyne, R. P. V. Localized Surface Plasmon Resonance Spectroscopy and Sensing. *Annual Review of Physical Chemistry* **2007**, *58*, 267–297.

7. Zhang, L.; Zhou, M.; Wang, A.; Zhang, T. Selective Hydrogenation over Supported Metal Catalysts: From Nanoparticles to Single Atoms. *Chemical Reviews* **2020**, *120*, 683–733.

8. Favier, I.; Pla, D.; Gmez, M. Palladium Nanoparticles in Polyols: Synthesis, Catalytic Couplings, and Hydrogenations. *Chemical Reviews* **2020**, *120*, 1146–1183.

9. Haruta, M.; Tsubota, S.; Kobayashi, T.; Kageyama, H.; Genet, M.; Delmon, B. Low-Temperature Oxidation of CO over Gold Supported on TiO_2, α-Fe_2O_3, and Co_3O_4. *Journal of Catalysis* **1993**, *144*, 175–192.

10. Zhang, Y.; Cui, X.; SHi, F.; Deng, Y. Nano-Gold Catalysis in Fine Chemical Synthesis. *Chemical Reviews* **2012**, *112*, 2467–2505.

11. Saavedra, J.; Doan, H. A.; Pursell, C. J.; Grabow, L. C.; Chandler, B. D. The Critical Role of Water at the Gold-Titania Interface in Catalytic CO Oxidation. *Science* **2008**, *345*, 1599–1602.

12. Clavero, C. Plasmon-Induced Hot-Electron Generation at Nanoparticle/Metal-Oxide Interfaces for Photovoltaic and Photocatalytic Devices. *Nature Photonics* **2014**, *8*, 95–103.

13. Le Ru, E. C.; Etchegoin, P. G. Single-Molecule Surface-Enhanced Raman Spectroscopy. *Annual Review of Physical Chemistry* **2012**, *63*, 65–87.

14. Mukherjee, S.; Libisch, F.; Large, N.; Neumann, O.; Brown, L. V.; Cheng, J.; Lassiter, J. B.; Carter, E. A.; Nordlander, P.; Halas, N. J. Hot Electrons Do the Impossible: Plasmon-Induced Dissociation of H_2 on Au. *Nano Letters* **2013**, *13*, 240–247.

15. Aslam, U.; Rao, V. G.; Chavel, S.; Linic, S. Catalytic Conversion of Solar to Chemical Energy on Plasmonic Metal Nanostructures. *Nature Catalysis* **2018**, *1*, 656–665.

16. Burns, E. N. V.; Lear, B. J. Controlled Rapid Formation of Polyurethane at 700 K: Thermodynamic and Kinetic Consequences of Extreme Photothermal Heating. *The Journal of Physical Chemistry C* **2019**, *123*, 14774–14780.

17. Widstrom, A. L.; Lear, B. J. Nanoscale Heat for Organic Transformations: A Photothermally Driven Retro Diels-Alder Reaction. *Applied Nanoscience* **2020**, *10*, 819–825.

18. Fortenbaugh, R. J.; Carrozzi, S. A.; Lear, B. J. Photothermal Control over the Mechanical and Physical Properties of Polydimethylsiloxane. *Macromolecules* **2019**, *52*, 3839–3844.

19. Steinhardt, R. C.; Steeves, T. M.; Wallace, B. M.; Moser, B.; Fishman, D. A.; Esser-Kahn, A. P. Photothermal Nanoparticle Initiation Enables Radical Polymerization and Yields Unique, Uniform Microfibers with Broad Spectrum Light. *ACS Applied Materials and Interfaces* **2017**, *9*, 39034–39039.

20. Govorov, A. O.; Richardson, H. H. Generating Heat with Metal Nanoparticles. *Nano Today* **2007**, *2*, 30–38.

21. An, K.; Somorjai, G. A. Size and Shape Control of Metal Nanoparticles for Reaction Selectivity in Catalysis. *ChemCatChem* **2012**, *4*, 1512–1524.

22. Guerrero-Martnez, A.; Barbosa, S.; Pastoriza-Santos, I.; Liz-Marzn, L. M. Nanostars Shine Bright for You: Colloidal Synthesis, Properties and Applications of Branched Metallic Nanoparticles. *Current Opinion in Colloid Interface Science* **2011**, *16*, 118 – 127.

23. Kinnear, C.; Moore, T. L.; Rodriguez-Lorenzo, L.; Rothen-Rutishauser, B.; Petri-Fink, A. Form Follows Function: Nanoparticle Shape and Its Implications for Nanomedicine. *Chemical Reviews* **2017**, *117*, 11476–11521.

24. Boles, M. A.; Engel, M.; Talapin, D. V. Self-Assembly of Colloidal Nanocrystals: From Intricate Structures to Functional Materials. *Chemical Reviews* **2016**, *116*, 11220–11289.

25. Yu, H.; Peng, Y.; Yang, Y.; LI, Z.-Y. Plasmon-Enhanced Light-Matter Interactions and Applications. *Computational Materials* **2019**, *5*, 45.

26. Halas, N. J.; Lal, S.; Chang, W.-S.; Link, S.; Nordlander, P. Plasmons in Strongly Coupled Metallic Nanostructures. *Chemical Reviews* **2011**, *111*, 3913–3961.

27. Ishida, T.; Murayama, T.; Taketoshi, A.; Haruta, M. Importance of Size and Contact Structure of Gold Nanoparticles for the Genesis of Unique Catalytic Processes. *Chemical Reviews* **2020**, *120*, 464–525.

28. Halperin, W. P. Quantum Size Effects in Metal Particles. *Review of Modern Physics* **1986**, *58*, 533–606.

29. Chakraborty, I.; Pradeep, T. Atomically Precise Clusters of Noble Metals: Emerging Link Between Atoms and Nanoparticles. *Chemical Reviews* **2017**, *117*, 8208–8271.

30. Jin, R.; Zeng, C.; Zhou, M.; Chen, Y. Atomically Precise Colloidal Metal Nanoclusters and Nanoparticles: Fundamentals and Opportunities. *Chemical Reviews* **2016**, *116*, 10346–10413.

31. Du, Y.; Sheng, H.; Astruc, D.; Zhu, M. Atomically Precise Noble Metal Nanoclusters as Efficient Catalysts: A Bridge Between Structure and Properties. *Chemical Reviews* **2020**, *120*, 526–622.

32. Agrachev, M.; Ruzzi, M.; Venzo, A.; Maran, F. Nuclear and Electron Magnetic Resonance Spectroscopies of Atomically Precise Gold Nanoclusters. *Accounts of Chemical Research* **2019**, *52*, 44–52.

33. Antonello, S.; Perera, N. V.; Ruzzi, M.; Gascn, J. A.; Maran, F. Interplay of Charge State, Lability, and Magnetism in the Molecule-Like $Au_{25}(SR)_{18}$ Cluster. *Journal of the American Chemical Society* **2013**, *135*, 15585–15594.

34. Agrachev, M.; Antonello, S.; Dainese, T.; Ruzzi, M.; Zoleo, A.; Apr, E.; Govind, N.; Fortunelli, A.; Sementa, L.; Maran, F. Magnetic Ordering in Gold Nanoclusters. *ACS Omega* **2017**, *2*, 2607–2617.

35. Antonello, S.; Arrigoni, G.; Dainese, T.; De Nardi, M.; Parisio, G.; Perotti, L.; Ren, A.; Venzo, A.; Maran, F. Electron Transfer through 3D Monolayers on Au_{25} Clusters. *ACS Nano* **2014**, *8*, 2788–2795.

36. Malola, S.; Kaappa, S.; Häkkinen, H. Role of Nanocrystal Symmetry in the Crossover Region from Molecular to Metallic Gold Nanoparticles. *The Journal of Physical Chemistry C* **2019**, *123*, 20655–20663.

37. Wang, C.; Daimon, H.; Onodera, T.; Koda, T.; Sun, S. A General Approach to the Size- and Shape-Controlled Synthesis of Platinum Nanoparticles and Their Catalytic Reduction of Oxygen. *Angewandte Chemie International Edition* **2008**, *47*, 3588–3591.

38. Demortire, A.; Launois, P.; Goubet, N.; Albouy, P.-A.; Petit, C. Shape-Controlled Platinum Nanocubes and Their Assembly into Two-Dimensional and Three-Dimensional Superlattices. *The Journal of Physical Chemistry B* **2008**, *112*, 14583–14592.

39. Brust, M.; Walker, M.; Bethell, D.; Schiffrin, D. J.; Whyman, R. Synthesis of Thiol-Derivatised Gold Nanoparticles in a Two-Phase LiquidLiquid System. *J. Chem. Soc., Chem. Commun.* **1994**, 801–802.

40. Cirri, A.; Silakov, A.; Lear, B. J. Ligand Control over the Electronic Properties within the Metallic Core of Gold Nanoparticles. *Angewandte Chemie* **2015**, *254*, 11750–11753.

41. Cirri, A.; Silakov, A.; Jensen, L.; Lear, B. J. Chain Length and Solvent Control over the Electronic Properties of Alkanethiolate-Protected Gold Nanoparticles at the Molecule-to-Metal Transition. *Journal of the American Chemical Society* **2016**, *138*, 15987–15993.

42. Cirri, A.; Silakov, A.; Jensen, L.; Lear, B. J. Probing Ligand-Induced Modulation of Metallic States in Small Gold Nanoparticles Using Conduction Electron Spin Resonance. *Physical Chemistry Chemical Physics* **2016**, *18*, 25443–25451.

43. Edmonds, R. N.; Harrison, M. R.; Edwards, P. P. Conduction Electron Spin Resonance in Metallic Systems. *Annual Reports on the Progress of Chemistry* **1985**, *82*, 265–308.

44. Inagaki, Y.; Yonemura, H.; Sakai, N.; Makihara, Y.; Kawae, T.; Yamada, S. Magnetism of Gold Nanorods Probed Using Electron Spin Resonance. *Applied Physics Letters* **2016**, *109*, 072404.

45. Blundell, S. *Magnetism in Condensed Matter*; Oxford University Press: Oxford, UK, 2001.

46. Nealon, G. L.; Donnio, B.; Greget, R.; Kappler, J.-P.; Terazzi, E.; Gallani, J.-L. Magnetism in Gold Nanoparticles. *Nanoscale* **2012**, *4*, 5244–5258.

47. van Leeuwen, D. A.; van Ruitenbeek, J. M.; Schmid, G.; de Jongh, L. J. Size-Dependent Magnetisation of Pd Clusters and Colloids. *Physics Letters A* **1992**, *170*, 325–333.

48. Walter, J.; Hara, S.; Suzuki, M.; Suzuki, L. S. In *Molecular Low Dimensional and Nanostructured Materials for Advanced Applications*; Graja, A., Bułka, B. R., Kajzar, F., Eds.; Springer Netherlands: Dordrecht, 2002; pp 329–333.

49. Wijn, H. P. J. *Magnetic Properties of Metals: d-Elements, Alloys and Compounds*; Springer Science & Business Media: Berlin, 2012.

50. Albert, H. J.; Rubin, L. R. *Platinum Group Metals and Compounds*; American Chemical Society: Washington, DC, 1971; Chapter 1, pp 1–16.

51. Dyson, F. J. Electron Spin Resonance Absorption in Metals II. Theory of Electron Diffusion and Skin Effect. *Physical Review* **1955**, *98*, 349–359.

52. Blundell, J. R. *Transition Ion Electron Paramagnetic Resonance*; Carendon Press: Oxford, UK, 1990.

53. Akaike, H. A New Look at the Statistical Model Identification. *IEEE Transactions on Automatic Control* **1974**, *19*, 716–723.

54. Burnham, K. P.; Anderson, D. R. Multimodel Inference: Understanding AIC and BIC in Model Selection. *Sociological Methods & Research* **2004**, *33*, 261–304.

55. Murtaugh, P. A. In Defense of P Values. *Ecology 95*, 611–617.

56. Jensen, C.; Buck, D.; Dilger, H.; Bauer, M.; Phillipp, F.; Roduner, E. Maximum Hydrogen Chemisorption on KL Zeolite Supported Pt Clusters. *Chem. Commun.* **2013**, *49*, 588–590.

57. Koseki, S.; Matsunaga, N.; Asada, T.; Schmidt, M. W.; Gordon, M. S. Spin-Orbit Coupling Constants in Atoms and Ions of Transition Elements: Comparison of Effective Core

Potentials, Model Core Potentials, and All-Electron Methods. *The Journal of Physical Chemistry A* **2019**, *123*, 2325–2339.

58. Häkkinen, H. The Gold-Sulphur Interface at the Nanoscale. *Nature Chemistry* **2012**, *4*, 443–455.

59. Horng, M. L.; Gardecki, J. A.; Papazyan, A.; Maroncelli, M. Subpicosecond Measurements of Polar Solvation Dynamics: Coumarin 153 Revisited. *The Journal of Physical Chemistry* **1995**, *99*, 17311–17337.

60. Hartland, G. V. Optical Studies of Dynamics in Noble Metal Nanostructures. *Chemical Reviews* **2011**, *111*, 3858–3887.

61. Huang, Y.; Yao, T.; Sun, Z. H.; Wei, S. Q. X-ray Absorption Fine Structure Spectroscopy Studies of Thiol-Capped Copper Nanoparticles. *Journal of Physics: Conference Series* **2013**, *430*, 12033.

62. Rogers, S.; Dimitratos, N.; Jones, W.; Bowker, M.; Kanaras, A. G.; Wells, P.; Catlow, C. R. A.; Parker, S. F. The Adsorbed State of a Thiol on Palladium Nanoparticles. *Physical Chemistry Chemical Physics* **2016**, *18*, 17265–17271.

63. Wikander, K.; Petit, C.; Holmberg, K.; Pileni, M.-P. Size Control and Growth Process of Alkylamine-Stabilized Platinum Nanocrystals: A Comparison between the Phase Transfer and Reverse Micelles Methods. *Langmuir* **2006**, *22*, 4863–4868.

64. Gavia, D. J.; Do, Y.; Gu, J.; Shon, Y.-S. Mechanistic Insights into the Formation of Dodecanethiolate-Stabilized Magnetic Iridium Nanoparticles: Thiosulfate *vs* Thiol Ligands. *The Journal of Physical Chemistry C* **2014**, *118*, 14548–14554.

Graphical TOC Entry